Development of a 3D Ni-Mn Binary Oxide Anode for Energy-Efficient Electro-Oxidation of Organic Pollutants

Keyvan Mirehbar [a], Jaime S. Sanchez [a], Sergio Pinilla [a], Freddy E. Oropeza [b], Ignasi Sirés [c], Víctor A. de la Peña O'Shea [b], Jesús Palma [a], Julio J. Lado [a,*]

[a] *Electrochemical Processes Unit, IMDEA Energy Institute, Avda. Ramón de la Sagra 3, 28935, Móstoles, Madrid, Spain*

[b] *Photoactivated Processes Unit, IMDEA Energy Institute, Avda. Ramón de la Sagra 3, 28935, Móstoles, Madrid, Spain*

[c] *Laboratori d'Electroquímica dels Materials i del Medi Ambient, Departament de Ciència de Materials i Química Física, Secció de Química Física, Facultat de Química, Universitat de Barcelona, Martí i Franquès 1-11, 08028 Barcelona, Spain*

Abstract

The depletion of clean water resources and the consequent accumulation of contaminants in aquatic systems must be urgently addressed by means of innovative solutions. Electro-oxidation (EO) is considered a promising technology, prized for its versatility and eco-friendliness. However, the excessively high prices and the toxicity associated with some of the materials currently employed for EO impede its broader application. This study introduces cost-effective Ni-Mn binary oxide anodes prepared on Ni foam (NF) substrate. A scalable synthesis route that enables a 35-fold increase in the production of active material through a single optimization step has been devised. The synthesized binary oxide material underwent electrochemical characterization, and its effectiveness was assessed in an electrochemical flow-through cell, benchmarked against single Ni or Mn oxides and more conventional alternatives like boron-doped diamond (BDD) and dimensionally-stable anode (DSA). The novel binary oxide anode demonstrated exceptional performance, achieving complete removal of phenol at very low current density of 5 mA cm^{-2}, along with an 80 % of chemical oxygen demand (COD) decay within only 60 min. The NF/$NiMnO_3$ anode outperformed the BDD and DSA when using comparable projected surface areas, owing to its high porosity and ability to produce hydroxyl radicals, as confirmed from the degradation profiles in the presence of radical scavengers. Furthermore, GC/MS analysis served to elucidate the degradation pathways of phenol.

Keywords: Electrochemical advanced oxidation processes (EAOPs), Electrochemical oxidation (EO), High oxidation power anode, Multi-metal oxides, Organic contaminant.

GRAPHICAL ABSTRACT

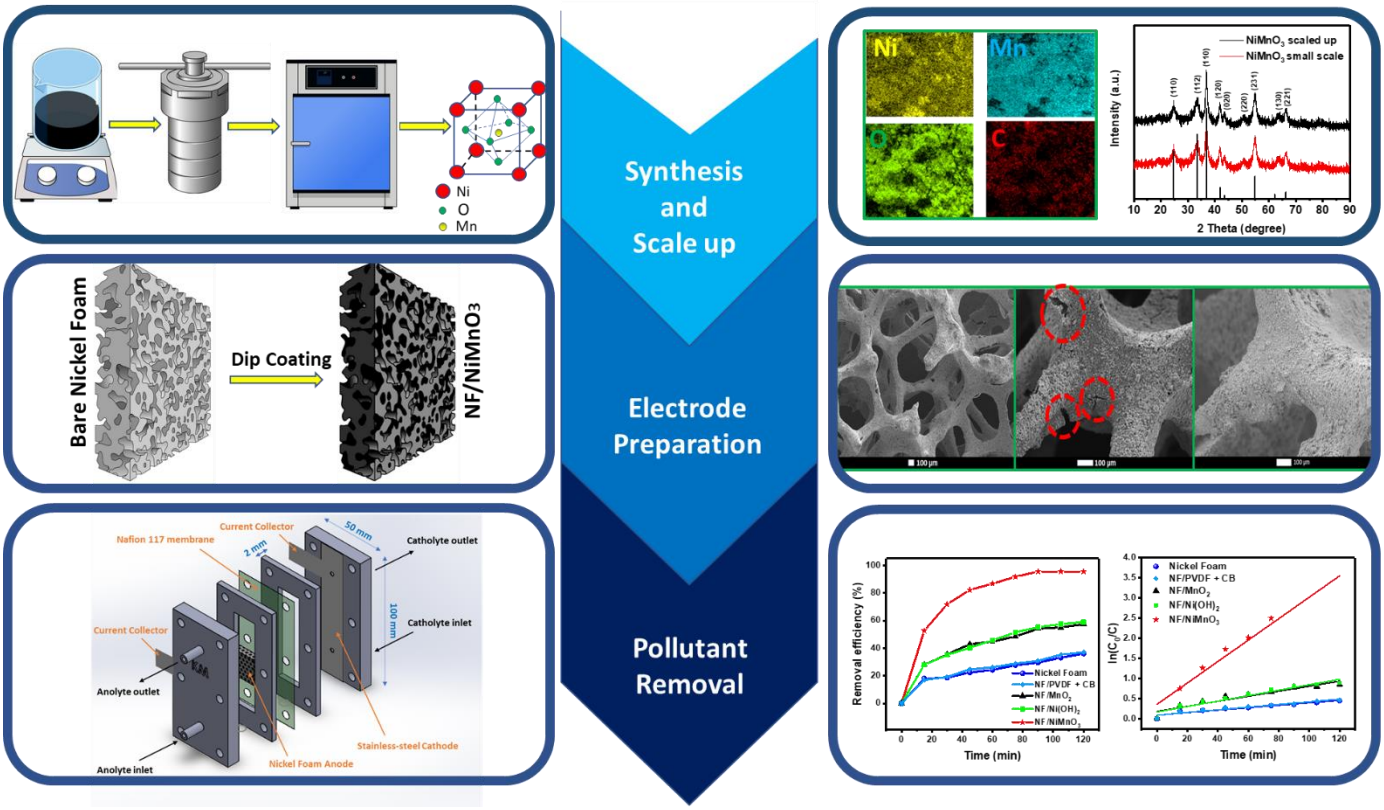

1. Introduction

The persistent introduction of organic pollutants into water systems from industrial, agricultural, and domestic activities is a pressing environmental concern, posing risks to both ecological systems and human health.[1] Emerging contaminants, which include complex industrial substances and everyday chemicals such as pharmaceuticals and personal care products, are not effectively tackled by traditional water treatment methods.[2] Within this context, the advanced oxidation processes (AOPs) become a viable solution,[3] wherein electrochemical AOPs (i.e., EAOPs) notably excel due to their efficiency and environmental compatibility.[4] EAOPs stand out for their ability to generate hydroxyl radicals (•OH), which effectively break down structurally complex contaminants into less harmful molecules.[5] In electro-oxidation (EO), a subset of EAOPs, an anode is employed to facilitate the production of these powerful oxidizing agents. However, the effectiveness of the EO process is critically dependent on the anode material. Traditional anodes like PbO_2, boron-doped diamond (BDD), SnO_2, dimensionally-stable anodes (DSA) and Ebonex have shown good performance[6], [7], [8], [9], [10], [11] but are marred by high costs, limited availability, and potential toxicity.[12], [13], [14] Therefore, there is a clear imperative for alternative materials that are both cost-effective and environmentally benign.

In response to this need, oxides based on Earth-abundant materials such as Ni and Mn have been identified as promising candidates.[15] The appeal of Ni and Mn lies in their capability to form binary oxides that can facilitate the production of hydroxyl radicals while minimizing side reactions like oxygen evolution. These binary oxides are advantageous due to their rich chemistry and multiple oxidation states, which are

instrumental in their oxygen evolution reaction (OER) activity.[15], [16], [17] $NiMnO_3$, in particular, combines the high catalytic activity of Mn with the conductivity of Ni, potentially outperforming their monometallic counterparts.[18] Based on these attractive characteristics, different Ni- and Mn-based oxide catalysts such as $NiMn_2O_4$ and $NiMnO_3$ have been widely studied for electrochemical energy storage and water splitting.[17] Nevertheless, to the best of the authors' knowledge, this research constitutes the pioneering investigation into the potential use of such type of bimetallic material in water treatment processes like EO.

Our study builds upon the premise that a synergistic combination of Ni and Mn in the form of a binary oxide, supported on a three-dimensional (3D) substrate like nickel foam (NF), could lead to an optimized EO process. We hypothesize that the multi-metallic nature and large porosity of NF/$NiMnO_3$ anodes will enhance their electrocatalytic performance, translating to more effective pollutant degradation with improved energy efficiency. This has been investigated by characterizing the electrochemical behavior of these electrodes and by evaluating their performance in terms of phenol degradation, since this molecule is a commonly encountered organic pollutant in wastewater. Additionally, the impact of operation parameters (i.e., current density, pH, flow rate and initial phenol concentration) on the decontamination process has been assessed. GC/MS analysis has served to elucidate the degradation pathways, aiming to advance our understanding of the mechanisms at play in water treatment by EO with this innovative material.

2. Experimental section

2.1. Electrode preparation

2.1.1. Synthesis and characterization of $NiMnO_3$

$NiMnO_3$ nanoparticles were synthesized via a facile hydrothermal process followed by thermal treatment based on a previously tested method (**Figure 1**).[19] One of the challenges for the synthesis of $NiMnO_3$ was the low yield of the process (3.7 %), which led to a small amount of the final product (20 mg of $NiMnO_3$). Since the preparation of electrodes consumes a relatively high amount of active material (approximately 2 g), the synthesis process was scaled-up from 25 mL of solution to 500 mL using a larger Teflon-lined stainless-steel autoclave reactor. By implementing this new process, the production was successfully increased to 800 mg, which represents a significant step forward multiplying the amount of product obtained by almost 35 times. X-ray diffraction (XRD) studies were performed to confirm the excellent agreement between the crystallinity patterns of the small- and large-scale products.

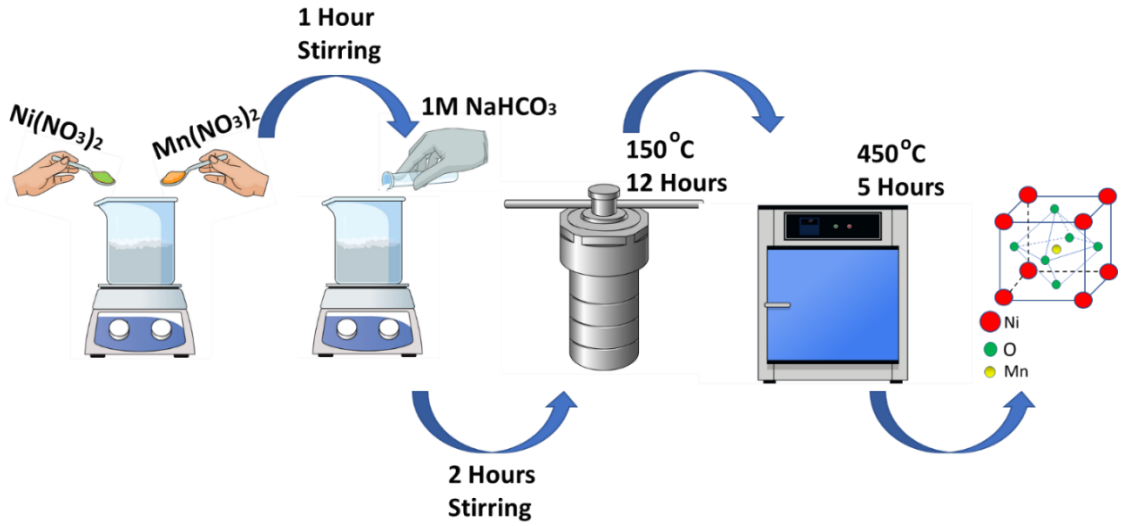

Figure 1. Schematic illustration of the synthesis of the $NiMnO_3$ nanoparticles.

The crystalline structure of the samples was analyzed by XRD using a PANalytical Empyream diffractometer with Kα radiation (λ = 1.54 Å) at a scan rate of 0.2 degrees s^{-}

[1], generated at 45 kV and an emission current of 40 mA. The specific surface area and pore size distribution of the samples were measured by the multipoint Brunnauer-Emmett-Teller (BET) and BJH analysis, respectively, from N_2 adsorption/desorption isotherms using a Quantachrome QuadraSorb-S equipment. X-ray photoelectron spectroscopy (XPS) was also conducted to analyze the surface of the samples utilizing a monochromatic Al radiation with an overall power of 50 W and energy resolution of 0.5 eV for high-resolution spectra, using SPEC PHOIBOS NAP-150 1D equipment.

2.1.2. Preparation and surface characterization of modified nickel foam electrodes

Nickel foam (20 ppi, 95 % porosity, Goodfellow) was used in this study as substrate material to incorporate different active materials (MnO_2, $Ni(OH)_2$ and $NiMnO_3$) onto its surface by a dip-coating procedure. The NF pieces were perfectly cut into dimensions of 20 mm × 20 mm × 6 mm (reproducible bare electrode mass of 1.2 ± 0.04 g). The pieces were subsequently washed with 0.1 M HCl, acetone, ethanol, and water under sonication, for 10 min each. The ink was prepared by mixing 85 % of the active material, 10 % of carbon black (CB, Ketjen Black EC-600 JD) as the conducting agent, and 5 % polyvinylidene fluoride (PVDF) as the binder in N-methyl-2-pyrrolidone. The NF pieces were then entirely submerged into the colloidal suspension for 30 min under sonication and dried at 80 ºC for 12 h. The mass loading of deposited particles over the NF obtained by this methodology was fairly constant (200 ± 5 mg). The morphologies of bare and modified NF were characterized by scanning electron microscopy (SEM) using a JEOL JSM-7800F Prime microscope at an acceleration voltage of 15 kV.

2.2. Electrochemical characterization of modified nickel foam electrodes

Electrochemical measurements were conducted in a standard three-electrode system, using Ag/AgCl (3 mol L^{-1} KCl) as the reference electrode and a platinum mesh as counter electrode. The electrochemical tests were performed with a Bio-Logic Science Instrument (VMP3) controlled with EC-Lab software. The OER potential was determined by linear sweep voltammetry (LSV) in 0.1 mol L^{-1} Na_2SO_4 solution. The potential between the working and reference electrodes was swept from 0.25 V to 2.5 V, at a scan rate of 10 mV s^{-1} The electrochemical impedance spectroscopy (EIS) test was conducted using a 0.1 mol L^{-1} Na_2SO_4 solution, with a frequency range of 100 kHz to 100 mHz and a disturbance amplitude of 5 mV.

2.3. Electro-oxidation process

2.3.1. Electrochemical cell

Figures 2a and **2b** show the 3D-printed electrochemical cell in the flow-through configuration, thus showing the electrolyte flow perpendicular to the flow of the electric current. The cell is made by 3D printing using resin (ANYCUBIC, 3D printing UV sensitive resin) material containing four blocks. The design of the electrochemical cell aimed at housing an NF electrode should allow uniform current and potential distribution, low ohmic internal resistance, and high rates of mass transport of the electroactive species to the electrode surface. This features can be achieved if the electrode surface is sufficiently thin for the voltage to be taken as constant and the distribution of the reaction current uniform over the electrode surface.[20]

In this configuration, the current collector (expanded graphite plate, Sigracell TF6) was placed into the inner blocks, holding the two-sided modified NF anode in the center of

the anolyte channel, whereas in the cathodic compartment, a stainless-steel plate (0.2 mm thickness, Goodfellow) was used as the electrode. The cell was connected to a peristaltic pump (Masterflex® L/S), which provided a constant flow rate through the cell. The interelectrode gap was of 4 mm, and a Nafion 117 membrane was added to separate the anolyte and catholyte.

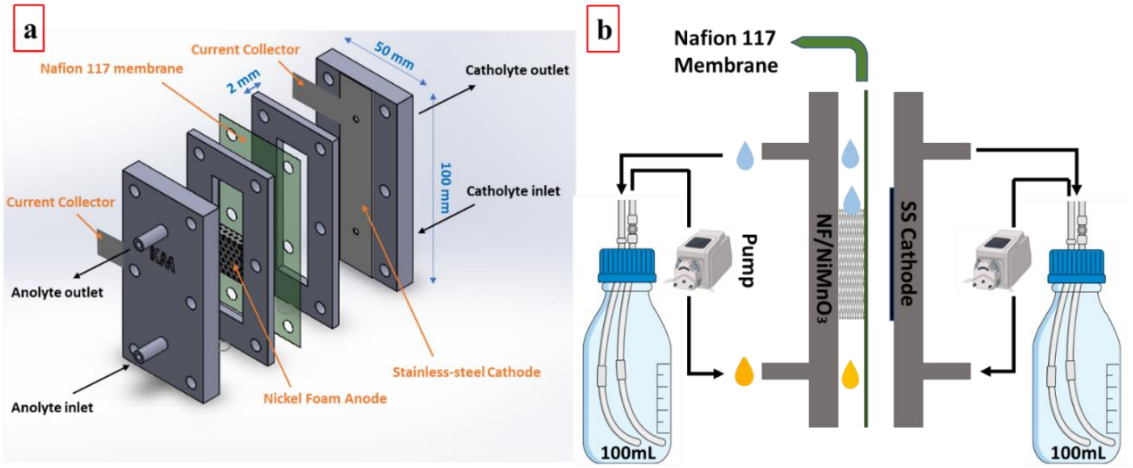

Figure 2. (a) Exploded view of 3D-printed electrochemical cell in the flow-through configuration. (b) Side view of the cell and scheme of the experimental setup.

2.3.2. Experimental setup

The electrochemical oxidation of phenol was carried out in 0.1 mol L^{-1} Na_2SO_4 as the supporting electrolyte. Different electrodes (bare NF, NF/MnO_2, NF/$Ni(OH)_2$ and NF/$NiMnO_3$) were used as anodes, always combined with a stainless-steel (SS) sheet as the cathode (**Figure 2b)**. Other experimental conditions were as follows: initial phenol concentration of 200 mg L^{-1}, anolyte and catholyte volume of 100 mL, flow rate of 30 mL min^{-1}, natural pH of the solution around 6.0. The electrochemical oxidation was subsequently optimized by evaluating the influence of different parameters such as the applied current density (5-20 mA cm^{-2}), initial pH value (from 3 to 11, using 0.1 M H_2SO_4

and NaOH solutions to adjust the initial value), flow rate (30-90 mL min^{-1}), and initial phenol concentrations (50-300 mg L^{-1}). Samples of 2 mL were periodically collected for analysis to follow the evolution of the phenol concentration and chemical oxygen demand (COD). After each phenol degradation experiment, the cell and the anode were cleaned by flowing MilliQ water for 1 h to remove the possible intermediate products. Moreover, the cathode was polished with sandpaper after each test.

2.3.3. Analytical methods

The COD of the solution was measured using commercial kits (Merck, ISO 15705) by Spectroquant® Prove 100 VIS spectrophotometer, whereas the phenol concentration was measured by UV/Vis spectroscopy on a Perkin-Elmer LAMBDA 1050 WB InGaAs UV/Vis spectrophotometer set at λ between 190 to 350 nm. The potential degradation pathway of phenol was assessed from the identification of intermediate compounds using high-performance gas chromatography-mass spectrometry (GC/MS). The organic intermediates were detected by an Agilent 5977B mass spectrometry equipped with an Agilent 8860 gas chromatograph (Agilent, US). An HP-5MS capillary column (30 m × 250 μm, 0.25μm) was used. The temperature was held at 40 ºC for 3 min, then increased at a rate of 3 ºC min^{-1} to 70 ºC and held at that temperature for 5 min, and again increased at a rate of 5 ºC min^{-1} from 75 ºC to 220 ºC.

3. Results and discussion

3.1.Crystal structures and morphologies of the electrodes

The structural properties and crystalline phase(s) of the samples obtained after thermal treatment (5 h at 450 ºC, **Figure 1**) in the synthesis process performed at small and large scales were analyzed by XRD and compared. As shown in **Figure 3a**, nine diffraction

peaks could be assigned in the $NiMnO_3$ samples, showing good agreement with crystal planes indexed to the rhombohedral ilmenite phase (the peaks from the JCPDS card no. 98-001-3753, space group: R-3, have been added to the figure).[21], [22] The XRD patterns of the product from the small and the large-scale synthesis do not exhibit significant differences, which validates the scaling-up methodology. This result poses a significant step forward for production of a large amount of active materials, which could pave the way to prepare electrodes of a larger size for industrial applications.

The N_2 adsorption-desorption isotherms **(Figure 3b)** and pore size distribution profiles (**Figure S1)** were plotted to explore the textural properties of the samples. As can be observed in **Figure 3b**, the analyzed samples displayed a type-IV isotherm showing hysteresis loops with different shapes, which suggests that those materials have different types of porosity. In the case of $NiMnO_3$, an H3-type hysteresis loop was observed; this means that the adsorption branch ascends continuously over the whole range of relative pressure, revealing the condensation of interparticle voids.[23] The specific surface area (S_{BET}) of $NiMnO_3$ nanoparticles was slightly higher (87 $m^2 g^{-1}$) than that of MnO_2 (78 $m^2 g^{-1}$), suggesting the presence of a larger number of potentially electroactive sites, which should lead to an improvement in the electrochemical performance.[24] The Barret-Joyner-Halenda (BJH) pore size distribution plot **(Figure S1)** shows the mesoporous nature (pore size below 15 nm) of the samples, in which the average diameter of the pores for $NiMnO_3$ nanoparticles (NPs) is centered at 8.2 nm.

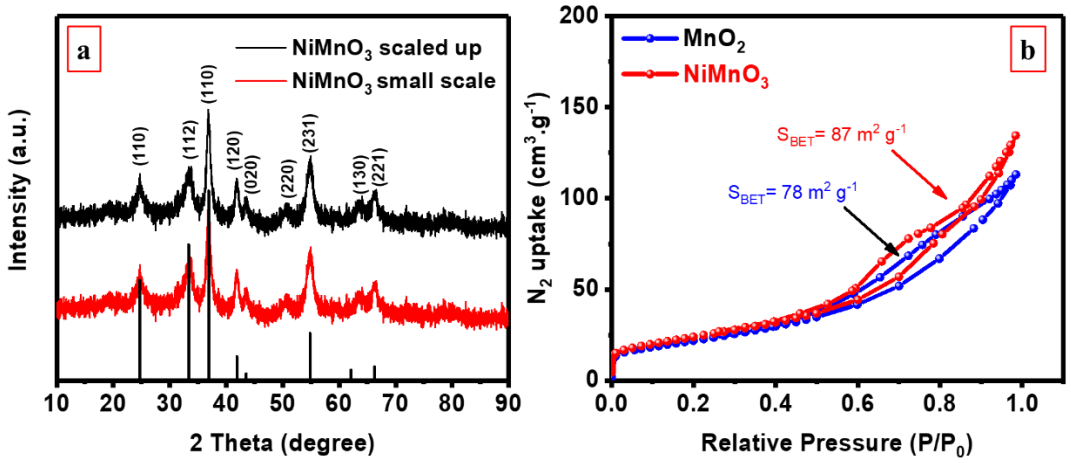

Figure 3. (a) XRD patterns of synthesized $NiMnO_3$. (b) N_2 adsorption-desorption isotherms of $NiMnO_3$ and MnO_2 nanoparticles.

The chemical composition and the oxidation state of the metals in the samples were evaluated by XPS (**Figure S2**). The strong overlap with Ni LMM Auger peaks makes difficult the interpretation of the Mn 2p region **(Figure S2a)**. Conversely, the Mn 3s spectrum (**Figure S2b**) has a multiplet split caused by the coupling of non-ionized 3s electrons with 3d valence-band electrons, which can be used for the analysis of the chemical state of Mn species.[25] The Mn 3s split is typically around 5.9 eV, 5.5 eV, and 4.8 eV for Mn^{2+}, Mn^{3+} and Mn^{4+}, respectively.[26] Since the split shown in **Figure S2a** is at 4.9 eV, the prevalence of Mn^{4+} in the $NiMnO_3$ sample can be assured, as expected for the Mn sites in the ilmenite structure.[27] There is a similar complex situation for the analysis of the Ni 2p region, since there is an overlap with Mn LMM Auger peaks. However, as shown in **Figure S2c**, it is reasonable to expect the Ni atoms to be as Ni^{2+} in our sample, in good agreement with the ilmenite structure of $NiMnO_3$.[28] **Figure S2d** shows the binding energy of O 1s displaying three peaks at 529 eV, 531 eV, and 534 eV. The former corresponds to the strongly bound lattice oxygen (O_L).[29] In contrast, the

highest binding energies were attributed to the weakly bound adsorbed oxygen (O_{ads}), including the hydroxyl group and water.[29] **Table 1** collects the contents of O_{ads} and O_L. The results indicate that both $NiMnO_3$ and MnO_2 might have a significant potential for organic pollutants oxidations since, according to previous studies,[30], [31], [32] the O_{ads} may be involved in the generation of active oxygen species ($^{\bullet}OH$), which are critical for EO application.

Table 1. XPS data showing the chemical states of oxygen on the NPs surface.

Sample	O 1s binding energy (eV)		Content (%)	
	O_L	O_{ads}	O_L	O_{ads}
$NiMnO_3$	529.67	531.19	64	36
MnO_2	529.48	531.06	66	31

The morphologies of bare and modified NF electrodes were characterized by SEM. Micrographies shown in **Figure 4** serve to corroborate the efficient deposition and homogeneous distribution of the metal oxide particles. The surface analysis of the modified NF confirms that dip coating is a suitable method to obtain a sufficiently uniform coating on the porous substrate. **Figure 4a-4c** display that the metal oxide coating is rough and the NPs are well distributed throughout the surface. According to the pictures, NF/MnO_2 **(Figure 4b)** presented less homogeneity compared to the synthesized NF/$NiMnO_3$ electrode **(Figure 4c-4d)**. It is expected that the lack of homogeneity and the large particle size might negatively impact the electrode performance by reducing the electrochemical surface area of the active material. Thus,

Figure 4b shows some cracks and defects on the surface of the MnO_2 electrode. This structure might provide a high resistance NiO layer similar to the one observed in the TiO_2 layer on Ti substrates, thereby yielding a shorter electrode lifespan, as well as the deactivation of the electrode.[33], [34]. On the other hand, the surface of the NF/$NiMnO_3$ electrode is more regular and compact, comprising uniform sphere-shaped particles with an average size of 500 nm to 1 µm in diameter. **Figure 4c-4d** also shows that the surface of the NF/$NiMnO_3$ was more integrated and the presence of the cracks decreased substantially. Furthermore, the EDS spectrum **(Figure S3)** and elemental mapping **(Figure 4e-4f),** showing the distribution of Ni, Mn, O and C in the NF/$NiMnO_3$ sample, revealed that Ni and Mn are uniformly distributed on the surface, thus confirming that the electrode surface was completely covered by the $NiMnO_3$ layer.

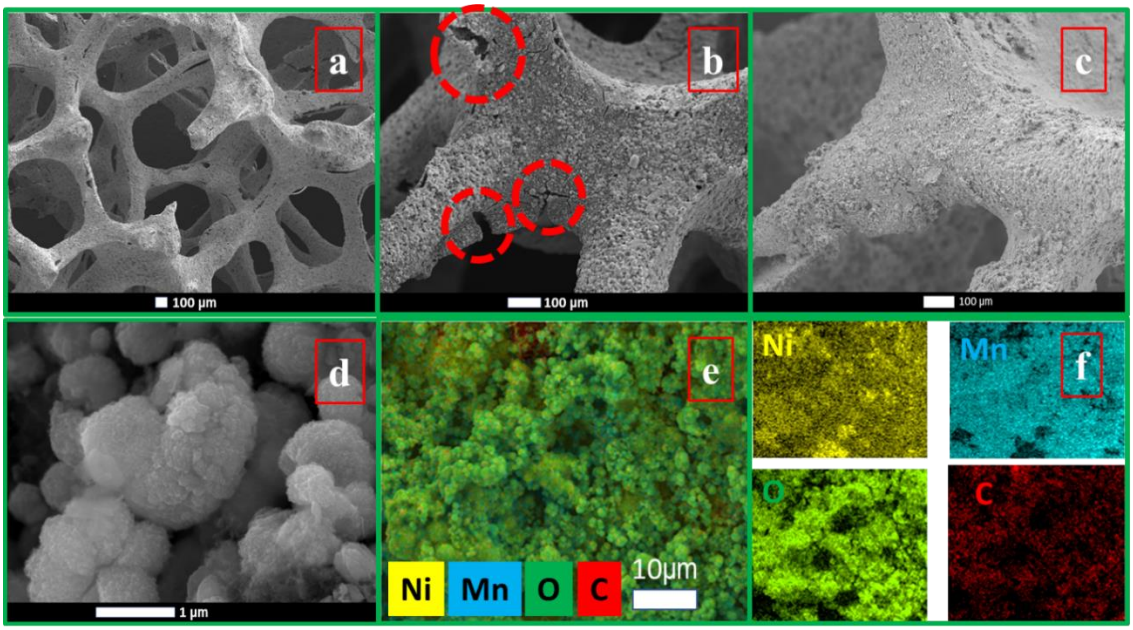

Figure 4. SEM images of different modified NF electrodes: (a) bare NF, (b) NF/MnO_2, (c, d) NF/$NiMnO_3$, at different magnifications. (e, f) Mapping of the different elements (Ni, Mn, O, and C) present in the NF/$NiMnO_3$ sample.

3.2. Electrochemical measurements

The prepared electrodes were characterized by LSV to determine the OER potential for each electroactive coating. The polarization curves (**Figure 5a**) show that the multi-metal oxide anode (NF/$NiMnO_3$) reached a substantially higher OER potential (2.10 vs. Ag/AgCl) as compared to the NF/MnO_2 and NF (1.75 V and 0.6 V vs. Ag/AgCl, respectively). In the literature, the OER overpotential has been commonly correlated with the oxidation capacity of the material, since the $^{\bullet}OH$ can thus be produced at a more oxidizing potential, and the competitive O_2 evolution is less favored than that occurring in so-called active anodes (e.g., IrO_2, RuO_2). The resulting radicals at NF/$NiMnO_3$ are expected to be more weakly bound, which will affect positively to the degradation of the organic contaminants.[35] Thus, the larger OER potential of the bimetallic oxide electrode compared to that of the NF and NF/MnO_2 serves as a first electrochemical indication of the superiority of the NF/$NiMnO_3$ for the EO process. Note that to design anodes that are ideal for generating adsorbed $^{\bullet}OH$ while inhibiting the O_2 generation at the anode surface, the intrinsic surface electronic configuration should be manipulated, eventually reducing the value of ΔG_{*OH}. Hence, the results reported here would support the strategy of designing multi-metal systems by tuning the electronic structure of the surface in such a way that the catalytic activity is improved for hydroxyl radical generation.[36], [37], [38] Note also that the small oxidation peaks observed in the $NiMnO_3$ curve between 1.5 V and 2.0 V can be primarily attributed to the redox transitions of Ni and Mn ions in the mixed oxide structure. Specifically, these peaks correspond to the successive oxidation processes involving the valence state changes of

Ni^{2+} to Ni^{3+}/Ni^{4+} and Mn^{3+} to Mn^{4+}, respectively. This analysis is also supported by the XPS analysis previously described.

Despite these findings, several researchers have recently argued that the OER potential should not be considered as the sole indicator of the ability to generate hydroxyl radicals. This is due to the different mechanisms followed by the OER (inner-sphere electron transfer) and the hydroxyl radical generation (outer-sphere electron transfer).[39], [40] Considering this approach, it has been established that the generation of hydroxyl radicals via desorption of OH* is necessary for viable EO systems. The Tafel slope (**Figure 5b**), which informs about the rate of current increase for a given electrochemical reaction, was used to compare the catalytic activity of the electrodes. A smaller Tafel slope suggests a faster reaction rate and a more efficient catalyst. As shown in **Figure 5b**, the $NF/NiMnO_3$ anode exhibits a smaller Tafel slope as compared to the NF/MnO_2 anode. A slope of 34 $mV\ dec^{-1}$ is consistent with a reaction mechanism that is limited by the adsorption of reactive intermediates on the electrode surface, suggesting that the initial electron transfer step is not the sole rate-determining factor. This value aligns well with the Butler-Volmer equation for a single-electron transfer process in the slow reaction rate limit, implying that subsequent steps, possibly involving the formation and evolution of oxygen species (in this case, hydroxyl radicals), play a significant role in the overall reaction kinetics. In light of this, the charge transfer mechanism for OER on the $NiMnO_3$ electrode can be inferred to involve multiple steps, including the adsorption of hydroxide ions, the formation of hydroxyl radicals, and the eventual evolution of molecular oxygen. The relatively small Tafel slope suggests favorable adsorption of intermediates and a

facilitated electron transfer process, underscoring the efficiency of the $NiMnO_3$ electrode as an EO catalyst.

Electrochemical impedance spectroscopy (EIS) measurements were further employed to reveal the catalytic properties of both anodes. As shown in **Figure S4**, EIS spectra show a semicircle, suggesting a charge transfer process during the OER. These Nyquist plots can be fitted by a 6-component equivalent electrical system.[41] **Figure S4** shows that the charge transfer resistance for $NF/NiMnO_3$ decreased in comparison with the NF/MnO_2. This result could be attributed to the primary effects of introducing a foreign metal, which is known as the ligand and strain effect.[42], [43], [44], [45], [46] The ligand effect consists of a charge transfer between neighboring metals that causes changes to the electronic structure. Charge transfer happens through shared oxygen ions due to the varied electron-donating properties of multi-metals, which in turn changes the electronic structure of the anode surface. The strain effect is the variation in the surface's lattice properties. The inclusion of foreign metals inevitably changes the lattice characteristics and, consequently, the amount of overlapping between atomic orbitals, thus changing the electronic structure. The ligand effect and the strain effect are typically indistinguishable, since they happen simultaneously in multi-metal oxides. Therefore, the modified electronic structure of multi-metal oxides is considered a comprehensive result of both effects.[18]

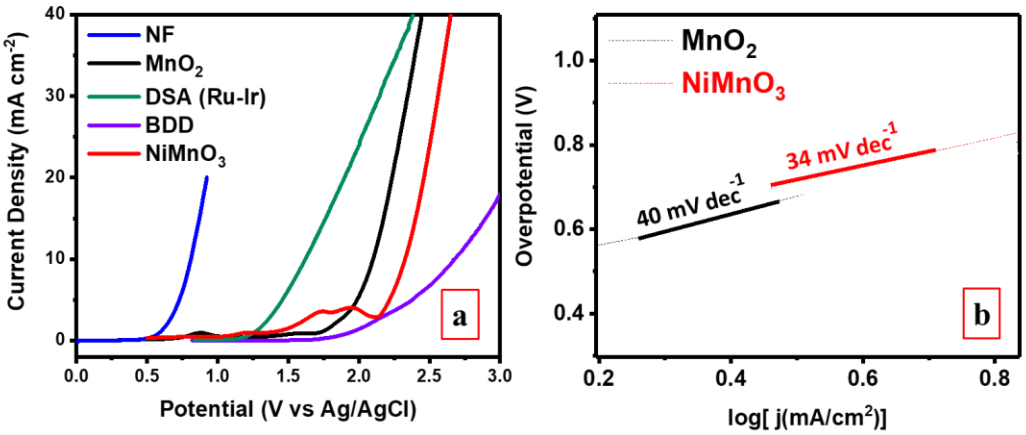

Figure 5. (a) LSV curves recorded with different electrodes. (b) Corresponding Tafel plots for NF/$NiMnO_3$ and NF/MnO_2.

3.3. Performance of multi-metal oxide for the electrocatalytic phenol removal

To evaluate the electrochemical degradation activity of the synthesized electrodes, phenol was chosen as the model pollutant for studying the EO process in the flow cell of **Figure 2**, using a 0.1 mol L^{-1} Na_2SO_4 solution as a supporting electrolyte. The results displayed in **Figure 6a** show that the NF/$NiMnO_3$ anode presents the highest phenol removal efficiency (90 % after 60 min, and overall degradation at 90 min) in comparison with NF/MnO_2, NF/$Ni(OH)_2$ and NF electrodes. The former two behaved similarly, attaining a removal of 60 % in 120 min, whereas bare NF anode was not very active (36 % at 120 min). To complete the analysis, **Figure 6b** shows the kinetic analysis of the phenol removals, informing about the superior kinetics developed by the NF/$NiMnO_3$ anode. Furthermore, the COD removal rates shown in **Figure 6c** point out that, as in the case of the phenol removal, NF/$NiMnO_3$ showed the best performance after 300 min of EO treatment (87 % COD removal), followed by NF/MnO_2 and NF/$Ni(OH)_2$ (64 %) and

bare NF (31 %). Additional data analysis of the samples revealed that the best average current efficiency (94 %) with the NF/$NiMnO_3$ electrode was achieved after 120 min, whereupon it gradually decreased, which can be explained by the accumulation of more refractory molecules like carboxylic acids.[47] That value contrasted with the 66 % reached after 120 min when the NF/MnO_2 electrode was tested. Therefore, considering all the data collected, one can conclude that the bimetallic oxide anode has a superior performance in comparison with the single oxides and the porous NF support.

The mechanism for phenol degradation was further studied taking into account that as the OER progresses, water molecules are oxidized to initially form adsorbed OH*.[48] At that point, depending on the adsorption energy of the electrode, either the OH* turns into O* or redox mediators (in this case, hydroxyl radicals) to oxidize the organic pollutants present in wastewater.[49] In principle, the adsorption energy of OH* is determined by the electronic structure of the anode surface.[50] Therefore, one could hypothesize that the introduction of a foreign metal in the oxide structure might modify the electronic structure, tuning the adsorption energies of the existing active sites in favor of a specific reaction pathway. To investigate the role of reactive oxygen species in the oxidation mechanism, *tert*-butanol (TBA) was employed as a selective hydroxyl radical scavenger. Furthermore, since methanol serves to quench both hydroxyl and sulfate radicals, additional experiments were performed spiking both solvents, and the results were compared with those obtained in the absence of scavengers **(Figure 6e)**. Adsorption experiments using both bare NF and NF/$NiMnO_3$ revealed a poor phenol removal efficiency of around 10 %, which suggests that the physical interactions provided by the high porosity have a limited contribution to the overall pollutant removal in EO process.

When methanol was introduced, the phenol removal rate was observed to be lower than 20 %. In contrast, the introduction of TBA, which is quite selective to scavenge hydroxyl radicals, resulted in a slightly higher removal efficiency of 30 %. These findings imply that hydroxyl radicals play a predominant role in the degradation of phenol in the absence of scavengers, with a smaller yet noticeable contribution from sulfate radicals (and other less active radicals). These experimental findings provide compelling evidence for the role of hydroxyl radicals (•OH) in the degradation process. The marked attenuation in phenol degradation efficiency observed in the presence of these scavengers underscores the significance of •OH radicals, substantiating the predominance of an indirect oxidation pathway.[51], [52], [53]

To benchmark the performance of our newly developed $NiMnO_3$ anode, **Figure 6f** presents a comparative analysis against commercial non-porous BDD and DSA plates, clearly highlighting the greater efficiency and potential advantages of our anode in EO processes. EO with BDD anode yielded approximately 50 % phenol removal after 120 minutes of treatment, while the use of DSA led to a poorer performance, with only about 20 % phenol removal under analogous conditions. Therefore, the NF/$NiMnO_3$ anode clearly outperformed the other two, not only surpassing them in terms of phenol degradation efficiency but also providing a faster decontamination. The superiority over the DSA can be readily explained from the much larger overpotential shown in **Figure 5a**. In the case of the much quicker degradation compared to EO with BDD, the overpotential cannot solely explain such difference, because the values for $NiMnO_3$ and BDD are similar. The fact that the NF/MnO_2 anode yielded a removal close to 60 % at 120 min (**Figure 6a**) despite its comparatively smaller overpotential (**Figure 5a**) allows

concluding that porous NF substrate, offering a large specific surface area with a great number of active sites, has a fundamental role. Therefore, the possibility of producing the new 3D bimetallic oxide anodes opens the door to overcome the limitations presented by conventional planar anodes.

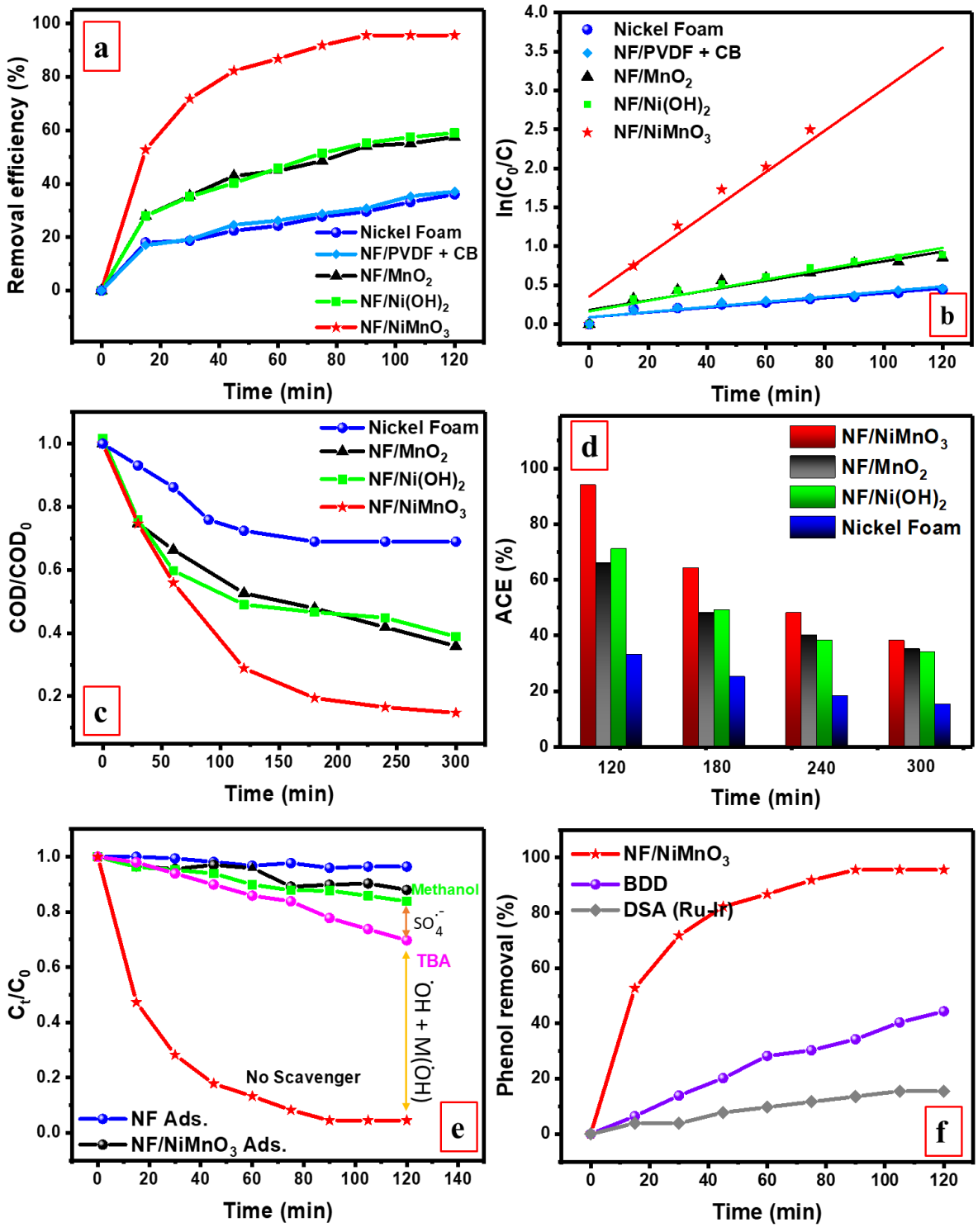

Figure 6. (a) Performance of the different anodes for 200 mg L^{-1} phenol removal, using

0.1 mol L^{-1} Na_2SO_4 electrolyte at pH 6.0 and current density of 5 mA cm^{-2}. (b) Corresponding pseudo-first-order kinetic analysis. (c) Corresponding normalized COD removal. (d) Average current efficiency. (e) Effect of the scavengers on the phenol concentration decay, along with adsorption trials. (f) Comparison of phenol degradation with three different anodes: commercial BDD and DSA, and new NF/$NiMnO_3$, all with the same projected area, under the conditions described in plot (a).

3.4. Optimization of EO process parameters

3.4.1. Effect of the applied current density

Current density is an essential parameter that determines the amount of hydroxyl radicals produced and the electron transfer rate, thus affecting the degradation rate of phenol.[54] **Figure 7a** displays the positive effect of increasing the current density (referred to the projected surface area of the anode) on COD removal. Thus, the increase from 2.5 to 20 mA cm^{-2} resulted in a better COD removal, increasing from 25 to 60 % after 60 min. A higher current density yields a greater amount of hydroxyl radicals, making it possible the simultaneous degradation of phenol and its reaction intermediates.[55] A gradual current increase implies the shift from charge transfer control to mass transport control.[56] Accordingly, when the current density exceeded 10 mA cm^{-2}, only a slight increase in the COD removal efficiency was observed. In addition, excessively high current densities result in the promotion of parasitic reactions, which have a negative impact on the Faradaic efficiency of hydroxyl radical generation. From these results, a current density of 10 mA cm^{-2} was used in the subsequent trials, aiming to achieve a high removal rate while minimizing the energy consumption.

3.4.2. Effect of the flow rate and solution pH

The influence of the flow rate (30, 60- and 90-mL min^{-1}) on the COD removal efficiency is displayed in **Figure 7b**. As can be observed, increasing the value from 30 to 60 mL min^{-1} caused a substantial rise in the COD decay (from 40 % to 70 % at 60 min). Nevertheless, the results suggest that no additional benefits in terms of COD removal can be attained at a higher value of 90 mL min^{-1}. The flow rate can affect the EO performance in several ways. First, it can affect the mixing of the reactants in the electrochemical cell.[57] If the flow rate is too low, there may not be enough turbulence inside the electrochemical cell to ensure an optimum mass transport of reactants. High stirring rates or liquid flow rates lead to fast solution homogenization, prevention of solid deposition, and assurance of proper transport towards the electrode surface. However, if the flow rate is too high, there may be excessive turbulence, leading to inefficient mixing and preferential paths, with insufficient residence time of organic molecules inside the cell.[58] Therefore, choosing an appropriate flow rate is critical. For the cell employed in this work, results obtained at 60 mL min^{-1} were superior.

On the other hand, the value of solution pH has influence on several factors, such as the type of oxidizing species and their oxidizing ability.[59] **Figure 7c** shows that the maximum COD removal efficiency was obtained at pH 6.0, which is the natural pH of the solution. This result can be explained based on the idea that the oxidation potential of $^{\bullet}OH$ decreases with increasing pH.[60] In addition, the OER potential decreases with an increase in pH; a higher OER potential value under acidic conditions weakens the parasitic oxygen evolution , thereby favoring the indirect catalytic degradation of phenol by hydroxyl radicals.[61]

3.4.3. Effect of the initial phenol concentration

From an engineering perspective, it is important to analyze the effect of the initial concentration of phenol on the degradation efficiency. As shown in **Figure 7d**, the highest COD removal efficiency was achieved when the initial concentration of phenol was 300 mg L^{-1}. As the initial concentration decreased from 300 mg L^{-1} to 50 mg L^{-1}, the COD removal efficiency decreased from 90 % to 70 %. However, it is important to pay attention not only to the COD removal efficiency but also to the average current efficiency (ACE). When designing a system, the balance between the applied current density and the initial concentration of the pollutant should be considered, otherwise, the lack of alignment between both parameters might cause inefficiency in the system. In the case of low initial concentrations (50 mg L^{-1}), it should be noted that although the total phenol removal can be achieved rapidly at 10 mA cm^{-2}, the average current density becomes quite low after only 120 min of the EO treatment (47 %). On the other hand, the optimized current density (10 mA cm^{-2}) seems to be insufficient to remove phenol and its intermediates in the case of high initial concentration (300 mg L^{-1}), as can be observed in **Figure 7d**. This situation leads to a longer process, which means higher energy consumption and higher cost. As can be seen, the best balance between COD removal efficiency, ACE, and duration of the process was achieved at 100 mg L^{-1} phenol concentration (100 % phenol removal in less than 60 min and 80 % COD removal and ACE of 64 % in 180 min).

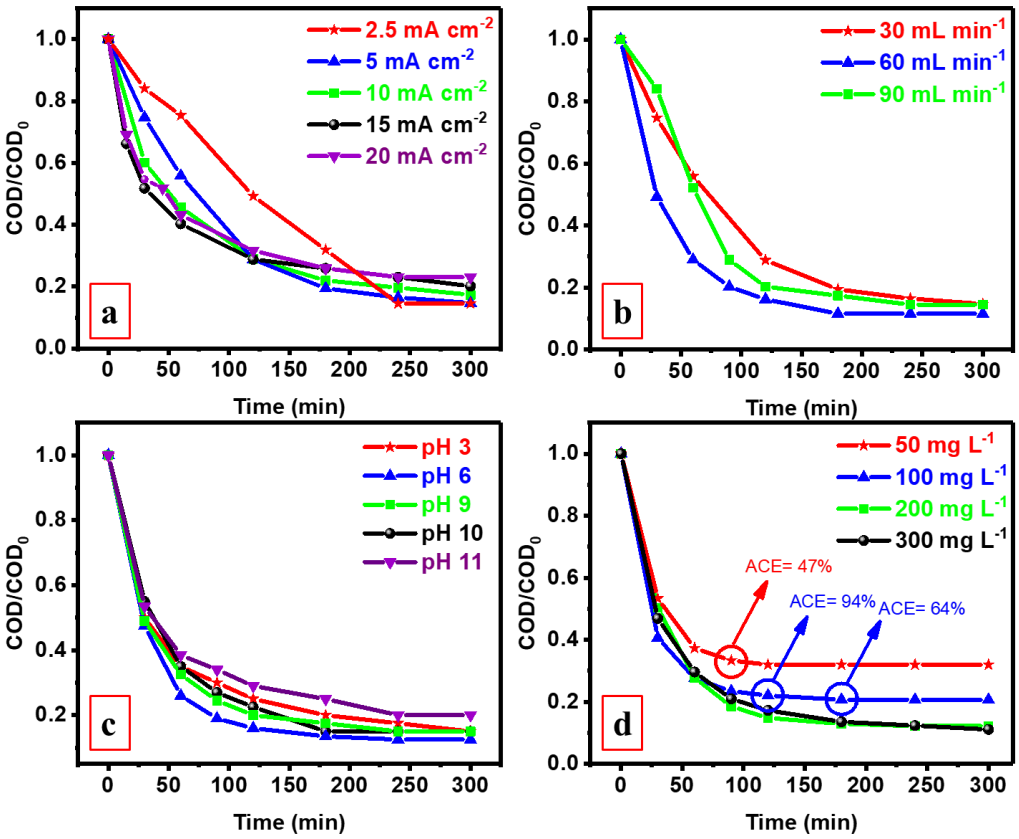

Figure 7. Effect of (a) current density (pH 6.0, flow rate of 30 mL min^{-1}, phenol concentration of 200 mg L^{-1}), (b) flow rate (current density of 10 mA cm^{-2}, pH 6.0, phenol concentration of 200 mg L^{-1}), (c) initial pH (current density of 10 mA cm^{-2}, flow rate of 60 mL min^{-1}, phenol concentration of 200 mg L^{-1}), and (d) initial phenol concentration (current density of 10 mA cm^{-2}, flow rate of 60 mL min^{-1}, pH 6.0) on COD removal efficiency.

According to the results, under the optimized operation conditions (current density of 10 mA cm^{-2}, flow rate of 60 mL min^{-1}, initial pH of 6.0, and initial concentration of 100 mg L^{-1}), the removal of phenol when treating 100 mL of solution (0.1 mol L^{-1} Na_2SO_4) reached 100 % in 60 min. Moreover, the COD removal rate was 80 % in 180 min. **Table 3** compares the results obtained with the NF/$NiMnO_3$ anode and those with other

electrodes studied by different researchers. NF/$NiMnO_3$ demonstrates an excellent performance, showcasing a removal efficiency of 100 % and 80 % within 60 min, for phenol and COD, respectively. These results highlight the effectiveness of the multi-metal oxide electrode, particularly the nickel manganese oxide ilmenite, as a promising option for efficient wastewater treatment in terms of organic pollutant removal.

Table 3. Comparison of the results obtained in this study with those of published works.

Compound	Anode type	Current density (mA cm^{-2})	Removal efficiency (in %)	Current efficiency (in %)	Ref.
Phenol	**NF/$NiMnO_3$**	**10**	**80 [COD]**	**64**	**This work**
Phenol	Ti/SnO_2-Sb_2O_3/MnO_2	15	38-59 [COD]	20-45	[62]
	Ti/SnO_2-Sb_2O_3/PbO_2				
	Ti/SnO_2-Sb_2O_3/RuO_2				
Phenol	Ti/SnO_2-Sb_2O_4-CNT	10	71 [COD]	-	[63]
Phenol	Ti/SnO_2-Sb_2O_5-RuO_2/α-PbO_2/β-PbO_2	10	94 [COD]	53	[64]
Phenol	Ebonex	2.5	95.3 [COD]	43.2	[65]

To provide a comprehensive understanding of the electrode stability, SEM analyses were performed before and after the electrochemical experiments **(Fig. S5-S7**).

Regarding the control electrode, composed of NF substrate coated with CB and PVDF, the morphological changes were studied to assess the potential degradation of the conductive agent and binder. The comparison between **Fig. S5** and **S7** reveals no substantial alteration in the morphology or structural integrity of the CB and PVDF, suggesting that these components are stable under the applied conditions. The absence of visible degradation underscores their robustness within the electrochemical environment. However, EDS analysis highlights a variation in the oxygen content, which was not initially anticipated. This increase is likely attributed to the oxidation of the NF substrate rather than the degradation of the CB or PVDF materials. Such an observation suggests that the primary electrochemical interactions and subsequent material transformations are predominantly occurring at the NF interface, with minimal impact on the stability of the other components under the examined operation conditions. On the other hand, for the NF/$NiMnO_3$ electrode, the comparison between **Fig. S3b** and **S6** reveals that the percentage of elements present on the electrode surface remained almost unaltered, with no remarkable changes. Moreover, the morphology of the NF/$NiMnO_3$ electrode was preserved, displaying no notable morphological alterations upon the electrolysis.

To evaluate the reusability of a freshly prepared NF/$NiMnO_3$ anode, five consecutive degradation tests were performed under optimal conditions. **Figure S8** illustrates the percentage of phenol removal at the end of each trial, evidencing that, despite a decline in activity, NF/$NiMnO_3$ anode still manages to eliminate 75 % of the phenol after five consecutive experiments (**Figure S8a)**. Kinetics analysis confirmed a slower degradation of phenol after the second experiment, although stabilizing the performance in the last three experiments (**Figure S8b)**. To investigate these changes in the performance, the

average cell voltage was analyzed trying to identify any sign of electrode degradation. The results displayed in **Figure S8c** showed no significant modification across consecutive tests or different time spans within each cycle. This outcome suggests consistent electric performance without evident signs of electrode corrosion despite reduced phenol degradation.

To further evaluate the electrode integrity, the mass of the electrode was measured after each consecutive experiment **(Figure S8d)**. The results revealed only a 5 % weight loss after 5 cycles, which could potentially contribute to the performance decline. However, no clear correlation was established between the loss of electrode weight and performance stability (for instance, despite the decrease of phenol removal between the second and the forth test, the weight of the electrode remained unchanged during those cycles). Therefore, this aspect requires further investigation.

As conclusion, it should be highlighted that, despite the initial decline of the performance, the NF/$NiMnO_3$ electrode exhibited stable kinetics and consistently high phenol removal values.

3.5. Analysis of the pathway for phenol degradation

To study the possible degradation pathways of phenol in the reaction process, UV–Vis spectroscopy and GC/MS were used to identify the intermediate products of phenol in the treated solutions **(Figure 8)**. The electrochemical degradation pathway of phenol typically involves the formation of several intermediate compounds, including hydroquinone (dihydroxybenzene molecule formed via oxidation of phenol at the anode) and benzoquinone. The results from UV-Vis shown in **Figure S9** display how the two absorbance peaks centered at 210 and 270 nm that correspond to the phenol decreased at

longer times of operation until it completely disappeared after 60 min. Simultaneously, during the degradation process, three additional peaks appeared according to the UV-Vis results (230-250 nm, 250-260 nm, and a very small 280-290 nm) which can be associated to a mixture of benzoquinone, hydroquinone, and catechol as intermediates of phenol degradation.[66], [67], [68] Additional results from GC/MS displayed in **Figure S10** show that major intermediates include benzoquinone and hydroquinone. The formation of these molecules is due to the characteristic behavior of phenol as an electron-withdrawing group (•OH) and the generated hydroxyl radicals are preferentially electrophilically added to the para and ortho positions of phenol.[69] Strong oxidizing agents react with the hydrogen atoms of the -OH groups in the hydroquinone, withdrawing hydrogen atoms to generate benzoquinone. These intermediates later oxidized to small aliphatic acids (maleic acid, succinic acid, malonic acid, oxalic acid) through a ring-opening reaction.[70] These compounds are slowly mineralized into CO_2 and H_2O, as described in the literature.

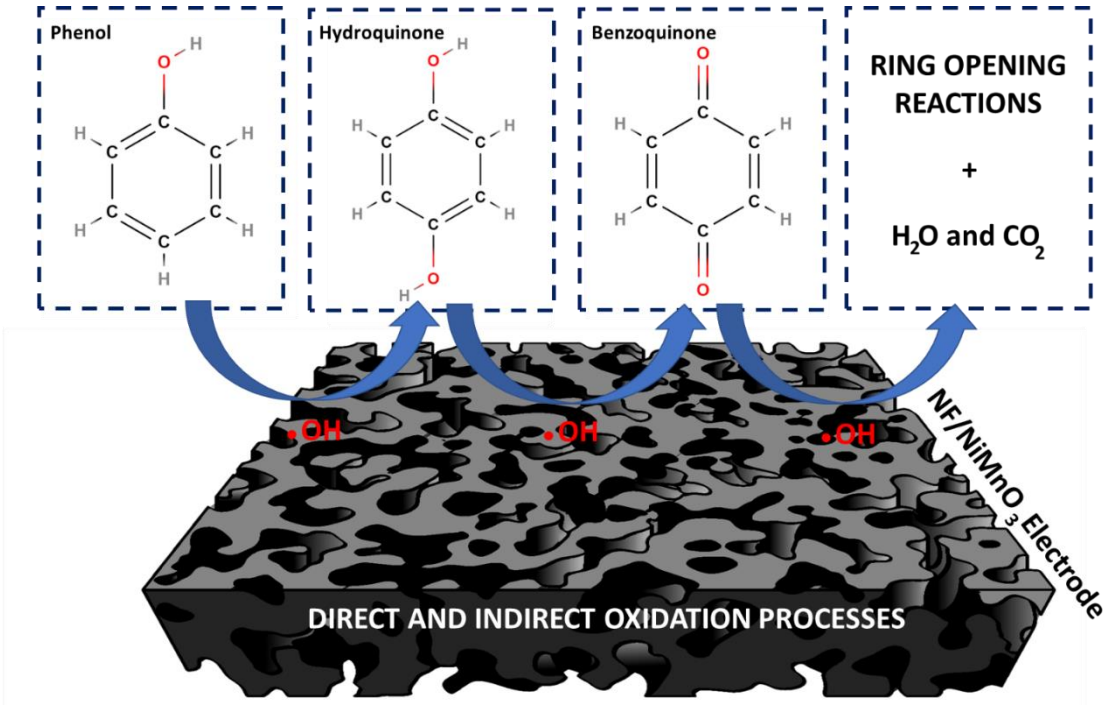

Figure 8. Potential degradation pathway from GC/MS results.

4. Conclusions

This study highlights the use of multi-metal oxide electrodes synthesized via a hydrothermal method for the electro-oxidation of organic pollutants in wastewater. Initially, this work shows the successful scaling up of the synthesis procedure of the bimetallic oxide material (35-fold increase), ensuring its practical viability for large-scale applications. A more favorable morphology and smaller particle size compared to electrodes composed of single metal oxides was revealed. $NiMnO_3$ exhibited an OER potential of 2.10 V vs Ag/AgCl, surpassing that of MnO_2. This enables a higher oxidation ability, making it particularly effective to degrade persistent organic compounds. Furthermore, EIS results confirmed a more facile charge transfer process for $NiMnO_3$ electrodes compared to its single-metal counterparts, suggesting lower resistance to electron transfer, eventually enhancing the electrocatalytic activity.

The integration of a 3D NF substrate and the design of the divided flow-through electrochemical cell plays a crucial role in enhancing mass transport and overall system performance. The 3D substrate provides a large surface area, enabling more active sites for pollutant oxidation. Additionally, the divided flow-through cell design effectively separates the anodic and cathodic reactions, preventing cross-contamination and allowing for targeted electrochemical processes. The NF/$NiMnO_3$ electrode achieved a 100 % phenol removal efficiency and 80 % COD reduction under optimized operation conditions, clearly outperforming the single-metal oxides and conventional electrodes (NF/MnO_2, BDD and DSA). This superiority can be attributed to its optimized morphology, increased oxidative potential, and efficient charge transfer characteristics. The mechanistic study, employing radical scavengers, elucidated that the predominant pathway for phenol degradation is indirect oxidation via hydroxyl radicals. This insight is crucial for tailoring the electrode and reaction conditions to maximize the generation and utilization of these reactive species.

The environmental implications of this research extend beyond the effective removal of organic pollutants. The improved mass transport and optimized electrochemical performance achieved with the multi-metal oxide electrode, in addition to the divided flow-through electrochemical cell design, offer possibilities for future applications to run additional reactions on the cathodic side, such as hydrogen (H_2) production, carbon dioxide (CO_2) reduction, or nitrogen (N_2) fixation. This hybrid cell opens avenues for sustainable and resource-efficient wastewater treatment systems.

Associated content

Supporting Information:

Removal rate calculations and material characterization.

Acknowledgments

K.M. acknowledges the HYSOLCHEM project (grant agreement No. 101017928) financed by the EU Horizon 2020 research and innovation programme "A Way of Making Europe". J. J. Lado appreciates the Talento's program of the Community of Madrid (Spain), which involves the project SELECTVALUE (2020-T1/AMB-19799). The authors also would like to thank Ignacio Almonacid for his assistance on 3D printing, Fernando Picó for collaborating in the SEM sample analysis, and Jennifer Cueto and Amir Jnaini for the discussions and assistance with the GC/MS analysis. I.S. gratefully acknowledges financial support from project PID2022-140378OB-I00 (MCIN/AEI/10.13039/501100011033, Spain), co-funded by the EU.

Author Information

Corresponding Author

Julio J. Lado – Electrochemical Processes Unit, IMDEA Energy Institute, Avda. Ramón de la Sagra 3, 28935, Móstoles, Madrid, Spain; Email: julio.lado@imdea.org

Authors

Keyvan Mirehbar – Electrochemical Processes Unit, IMDEA Energy Institute, Avda. Ramón de la Sagra 3, 28935, Móstoles, Madrid, Spain

Jaime S. Sanchez – Electrochemical Processes Unit, IMDEA Energy Institute, Avda. Ramón de la Sagra 3, 28935, Móstoles, Madrid, Spain

Sergio Pinilla – Electrochemical Processes Unit, IMDEA Energy Institute, Avda. Ramón de la Sagra 3, 28935, Móstoles, Madrid, Spain

Freddy E. Oropeza – Photoactivated Processes Unit, IMDEA Energy Institute, Avda. Ramón de la Sagra 3, 28935, Móstoles, Madrid, Spain

Ignasi Sirés – Laboratori d'Electroquímica dels Materials i del Medi Ambient, Departament de Ciència de Materials i Química Física, Secció de Química Física, Facultat de Química, Universitat de Barcelona, Martí i Franquès 1-11, 08028 Barcelona, Spain

Víctor de la Peña O.Shea – Photoactivated Processes Unit, IMDEA Energy Institute, Avda. Ramón de la Sagra 3, 28935, Móstoles, Madrid, Spain

Jesús Palma – Electrochemical Processes Unit, IMDEA Energy Institute, Avda. Ramón de la Sagra 3, 28935, Móstoles, Madrid, Spain

References

[1] N. E. Peters, M. Meybeck, and D. V. Chapman, "Effects of Human Activities on Water Quality," in *Encyclopedia of Hydrological Sciences*, M. G. Anderson and J. J. McDonnell, Eds., Chichester, UK: John Wiley & Sons, Ltd, 2005, p. hsa096. doi: 10.1002/0470848944.hsa096.

[2] S. Sharma and A. Bhattacharya, "Drinking water contamination and treatment techniques," *Appl. Water Sci.*, vol. 7, no. 3, pp. 1043–1067, Jun. 2017, doi: 10.1007/s13201-016-0455-7.

[3] M. A. Oturan and J.-J. Aaron, "Advanced Oxidation Processes in Water/Wastewater Treatment: Principles and Applications. A Review," *Crit. Rev. Environ. Sci. Technol.*, vol. 44, no. 23, pp. 2577–2641, Dec. 2014, doi: 10.1080/10643389.2013.829765.

[4] F. C. Moreira, R. A. R. Boaventura, E. Brillas, and V. J. P. Vilar, "Electrochemical advanced oxidation processes: A review on their application to synthetic and real wastewaters," *Appl. Catal. B Environ.*, vol. 202, pp. 217–261, Mar. 2017, doi: 10.1016/j.apcatb.2016.08.037.

[5] M. Panizza and G. Cerisola, "Direct And Mediated Anodic Oxidation of Organic Pollutants," *Chem. Rev.*, vol. 109, no. 12, pp. 6541–6569, Dec. 2009, doi: 10.1021/cr9001319.

[6] J. Zambrano and B. Min, "Electrochemical treatment of leachate containing highly concentrated phenol and ammonia using a Pt/Ti anode at different current densities," *Environ. Technol. Innov.*, vol. 18, p. 100632, May 2020, doi: 10.1016/j.eti.2020.100632.

[7] Y. Yao, C. Huang, Y. Yang, M. Li, and B. Ren, "Electrochemical removal of thiamethoxam using three-dimensional porous PbO_2-CeO_2 composite electrode: Electrode characterization, operational parameters optimization and degradation pathways," *Chem. Eng. J.*, vol. 350, pp. 960–970, Oct. 2018, doi: 10.1016/j.cej.2018.06.036.

[8] Y. Wang, B. Gu, and W. Xu, "Electro-catalytic degradation of phenol on several metal-oxide anodes," *J. Hazard. Mater.*, vol. 162, no. 2–3, pp. 1159–1164, Mar. 2009, doi: 10.1016/j.jhazmat.2008.05.164.

[9] N. Yang *et al.*, "Conductive diamond: synthesis, properties, and electrochemical applications," *Chem. Soc. Rev.*, vol. 48, no. 1, pp. 157–204, 2019, doi: 10.1039/C7CS00757D.

[10] Y. He, H. Lin, Z. Guo, W. Zhang, H. Li, and W. Huang, "Recent developments and advances in boron-doped diamond electrodes for electrochemical oxidation of organic pollutants," *Sep. Purif. Technol.*, vol. 212, pp. 802–821, Apr. 2019, doi: 10.1016/j.seppur.2018.11.056.

[11] W. Wu, Z.-H. Huang, and T.-T. Lim, "Recent development of mixed metal oxide anodes for electrochemical oxidation of organic pollutants in water," *Appl. Catal. Gen.*, vol. 480, pp. 58–78, Jun. 2014, doi: 10.1016/j.apcata.2014.04.035.

[12] R. KStz, H. Neff, and S. Stucki, "Anodic Iridium Oxide Films," *J Electrochem Soc*, vol. 131.

[13] R. Kötz, H. J. Lewerenz, P. Brüesch, and S. Stucki, "Oxygen evolution on Ru and Ir electrodes," *J. Electroanal. Chem. Interfacial Electrochem.*, vol. 150, no. 1–2, pp. 209–216, Jul. 1983, doi: 10.1016/S0022-0728(83)80203-4.

[14] S. Cherevko, "Oxygen and hydrogen evolution reactions on Ru, RuO_2, Ir, and IrO_2 thin film electrodes in acidic and alkaline electrolytes: A comparative study on activity and stability," *Catal. Today*, 2016.

[15] A. Singh, R. Tejasvi, S. Karmakar, and S. Basu, "α-Fe_2O_3 nanorods decorated with $NiMnO_3$ co-catalyst as photoanode for enhanced oxygen evolution reaction in photoelectrochemical water splitting," *Mater. Today Commun.*, vol. 27, p. 102231, Jun. 2021, doi: 10.1016/j.mtcomm.2021.102231.

[16] Y. H. Ahmad, K. A. Eid, S. Y. AlQaradawi, and N. K. Allam, "Highly active, durable and pH-universal hybrid oxide nanocrystals for efficient oxygen evolution," *Sustain. Energy Fuels*, vol. 1, no. 5, pp. 1123–1129, 2017, doi: 10.1039/C7SE00111H.

[17] X. He *et al.*, "$NiMnO_3$/$NiMn_2O_4$ Oxides Synthesized via the Aid of Pollen: Ilmenite/Spinel Hybrid Nanoparticles for Highly Efficient Bifunctional Oxygen Electrocatalysis," *ACS Appl. Mater. Interfaces*, vol. 8, no. 40, pp. 26740–26757, Oct. 2016, doi: 10.1021/acsami.6b08101.

[18] J. S. Kim, B. Kim, H. Kim, and K. Kang, "Recent Progress on Multimetal Oxide Catalysts for the Oxygen Evolution Reaction," *Adv. Energy Mater.*, vol. 8, no. 11, p. 1702774, Apr. 2018, doi: 10.1002/aenm.201702774.

[19] J. S. Sanchez, A. Pendashteh, J. Palma, M. Anderson, and R. Marcilla, "Synthesis and application of $NiMnO_3$-rGO nanocomposites as electrode materials for hybrid energy storage devices," *Appl. Surf. Sci.*, vol. 460, pp. 74–83, Dec. 2018, doi: 10.1016/j.apsusc.2018.02.165.

[20] J. M. Friedrich, C. Ponce-de-León, G. W. Reade, and F. C. Walsh, "Reticulated vitreous carbon as an electrode material," *J. Electroanal. Chem.*, vol. 561, pp. 203–217, Jan. 2004, doi: 10.1016/j.jelechem.2003.07.019.

[21] P. Kakvand *et al.*, "Synthesis of $NiMnO_3$/C nano-composite electrode materials for electrochemical capacitors," *Nanotechnology*, vol. 27, no. 31, p. 315401, Aug. 2016, doi: 10.1088/0957-4484/27/31/315401.

[22] W. H. Cloud, "Crystal Structure and Ferrimagnetism in $NiMnO_3$ and $CoMnO_3$," *Phys. Rev.*, vol. 111, no. 4, pp. 1046–1049, Aug. 1958, doi: 10.1103/PhysRev.111.1046.

[23] T. Horikawa, D. D. Do, and D. Nicholson, "Capillary condensation of adsorbates in porous materials," *Adv. Colloid Interface Sci.*, vol. 169, no. 1, pp. 40–58, Nov. 2011, doi: 10.1016/j.cis.2011.08.003.

[24] F. G. Davia, C. C. Fernández, F. J. Williams, and E. J. Calvo, "Effect of porosity and active area on the assessment of catalytic activity of non-precious metal electrocatalyst for oxygen reduction," *J. Phys. Condens. Matter*, vol. 33, no. 32, p. 324001, Aug. 2021, doi: 10.1088/1361-648X/ac0382.

[25] V. R. Galakhov *et al.*, "Mn 3s exchange splitting in mixed-valence manganites," *Phys. Rev. B*, vol. 65, no. 11, p. 113102, Feb. 2002, doi: 10.1103/PhysRevB.65.113102.

[26] J. L. Junta and M. F. Hochella, “Manganese (II) oxidation at mineral surfaces: A microscopic and spectroscopic study,” *Geochim. Cosmochim. Acta*, vol. 58, no. 22, pp. 4985–4999, Nov. 1994, doi: 10.1016/0016-7037(94)90226-7.
[27] M. C. Biesinger, B. P. Payne, A. P. Grosvenor, L. W. M. Lau, A. R. Gerson, and R. St. C. Smart, “Resolving surface chemical states in XPS analysis of first row transition metals, oxides and hydroxides: Cr, Mn, Fe, Co and Ni,” *Appl. Surf. Sci.*, vol. 257, no. 7, pp. 2717–2730, Jan. 2011, doi: 10.1016/j.apsusc.2010.10.051.
[28] A. P. Grosvenor, M. C. Biesinger, R. St. C. Smart, and N. S. McIntyre, “New interpretations of XPS spectra of nickel metal and oxides,” *Surf. Sci.*, vol. 600, no. 9, pp. 1771–1779, May 2006, doi: 10.1016/j.susc.2006.01.041.
[29] L. An, L. Huang, P. Zhou, J. Yin, H. Liu, and P. Xi, “A Self-Standing High-Performance Hydrogen Evolution Electrode with Nanostructured $NiCo_2O_4$/CuS Heterostructures,” *Adv. Funct. Mater.*, vol. 25, no. 43, pp. 6814–6822, Nov. 2015, doi: 10.1002/adfm.201503784.
[30] X. Fu, Y. Han, H. Xu, Z. Su, and L. Liu, “Electrochemical study of a novel high-efficiency PbO_2 anode based on a cerium-graphene oxide co-doping strategy: Electrodeposition mechanism, parameter optimization, and degradation pathways,” *J. Hazard. Mater.*, vol. 422, p. 126890, Jan. 2022, doi: 10.1016/j.jhazmat.2021.126890.
[31] L. Zhang, L. Xu, J. He, and J. Zhang, “Preparation of Ti/SnO_2-Sb electrodes modified by carbon nanotube for anodic oxidation of dye wastewater and combination with nanofiltration,” *Electrochimica Acta*, vol. 117, pp. 192–201, Jan. 2014, doi: 10.1016/j.electacta.2013.11.117.
[32] Y. Chen *et al.*, “Preparation and characterization of TiO_2-NTs/SnO_2-Sb electrodes by electrodeposition,” *J. Electroanal. Chem.*, vol. 648, no. 2, pp. 119–127, Oct. 2010, doi: 10.1016/j.jelechem.2010.08.004.
[33] G. Zhao *et al.*, “Fabrication and Electrochemical Treatment Application of A Novel Lead Dioxide Anode with Superhydrophobic Surfaces, High Oxygen Evolution Potential, and Oxidation Capability,” *Environ. Sci. Technol.*, vol. 44, no. 5, pp. 1754–1759, Mar. 2010, doi: 10.1021/es902336d.
[34] X. Li, D. Shao, H. Xu, W. Lv, and W. Yan, “Fabrication of a stable Ti/TiO_xH_y /Sb−SnO_2 anode for aniline degradation in different electrolytes,” *Chem. Eng. J.*, vol. 285, pp. 1–10, Feb. 2016, doi: 10.1016/j.cej.2015.09.089.
[35] C. A. Martinez-Huitle and S. Ferro, “Electrochemical Oxidation of Organic Pollutants for the Wastewater Treatment: Direct and Indirect Processes,” *ChemInform*, vol. 38, no. 14, Apr. 2007, doi: 10.1002/chin.200714276.
[36] Z. W. Seh, J. Kibsgaard, C. F. Dickens, I. Chorkendorff, J. K. Nørskov, and T. F. Jaramillo, “Combining theory and experiment in electrocatalysis: Insights into materials design,” *Science*, vol. 355, no. 6321, p. eaad4998, Jan. 2017, doi: 10.1126/science.aad4998.
[37] J. W. D. Ng *et al.*, “Gold-supported cerium-doped NiO_x catalysts for water oxidation,” *Nat. Energy*, vol. 1, no. 5, p. 16053, Apr. 2016, doi: 10.1038/nenergy.2016.53.
[38] O. Diaz-Morales, I. Ledezma-Yanez, M. T. M. Koper, and F. Calle-Vallejo, “Guidelines for the Rational Design of Ni-Based Double Hydroxide Electrocatalysts

for the Oxygen Evolution Reaction," *ACS Catal.*, vol. 5, no. 9, pp. 5380–5387, Sep. 2015, doi: 10.1021/acscatal.5b01638.
[39] R. Jaimes, J. Vazquez-Arenas, I. González, and M. Galván, "Theoretical evidence of the relationship established between the HO radicals and H_2O adsorptions and the electroactivity of typical catalysts used to oxidize organic compounds," *Electrochimica Acta*, vol. 229, pp. 345–351, Mar. 2017, doi: 10.1016/j.electacta.2017.01.120.
[40] A. H. Henke, T. P. Saunders, J. A. Pedersen, and R. J. Hamers, "Enhancing Electrochemical Efficiency of Hydroxyl Radical Formation on Diamond Electrodes by Functionalization with Hydrophobic Monolayers," *Langmuir*, vol. 35, no. 6, pp. 2153–2163, Feb. 2019, doi: 10.1021/acs.langmuir.8b04030.
[41] O. Shmychkova, T. Luk'yanenko, R. Amadelli, and A. Velichenko, "Electrodeposition of Ce-doped PbO_2," *J. Electroanal. Chem.*, vol. 706, pp. 86–92, Oct. 2013, doi: 10.1016/j.jelechem.2013.08.002.
[42] J. R. Kitchin, J. K. Nørskov, M. A. Barteau, and J. G. Chen, "Role of Strain and Ligand Effects in the Modification of the Electronic and Chemical Properties of Bimetallic Surfaces," *Phys. Rev. Lett.*, vol. 93, no. 15, p. 156801, Oct. 2004, doi: 10.1103/PhysRevLett.93.156801.
[43] Z. Xu and J. R. Kitchin, "Tuning oxide activity through modification of the crystal and electronic structure: from strain to potential polymorphs," *Phys. Chem. Chem. Phys.*, vol. 17, no. 43, pp. 28943–28949, 2015, doi: 10.1039/C5CP04840K.
[44] T. Bligaard and J. K. Nørskov, "Ligand effects in heterogeneous catalysis and electrochemistry," *Electrochimica Acta*, vol. 52, no. 18, pp. 5512–5516, May 2007, doi: 10.1016/j.electacta.2007.02.041.
[45] I. E. L. Stephens *et al.*, "Tuning the Activity of Pt(111) for Oxygen Electroreduction by Subsurface Alloying," *J. Am. Chem. Soc.*, vol. 133, no. 14, pp. 5485–5491, Apr. 2011, doi: 10.1021/ja111690g.
[46] F. Calle-Vallejo, M. T. M. Koper, and A. S. Bandarenka, "Tailoring the catalytic activity of electrodes with monolayer amounts of foreign metals," *Chem. Soc. Rev.*, vol. 42, no. 12, p. 5210, 2013, doi: 10.1039/c3cs60026b.
[47] M. A. Oturan, M. Pimentel, N. Oturan, and I. Sirés, "Reaction sequence for the mineralization of the short-chain carboxylic acids usually formed upon cleavage of aromatics during electrochemical Fenton treatment," *Electrochimica Acta*, vol. 54, no. 2, pp. 173–182, Dec. 2008, doi: 10.1016/j.electacta.2008.08.012.
[48] S. Siahrostami *et al.*, "A Review on Challenges and Successes in Atomic-Scale Design of Catalysts for Electrochemical Synthesis of Hydrogen Peroxide," *ACS Catal.*, vol. 10, no. 14, pp. 7495–7511, Jul. 2020, doi: 10.1021/acscatal.0c01641.
[49] X. Shi *et al.*, "Understanding activity trends in electrochemical water oxidation to form hydrogen peroxide," *Nat. Commun.*, vol. 8, no. 1, p. 701, Sep. 2017, doi: 10.1038/s41467-017-00585-6.
[50] J. K. Nørskov, T. Bligaard, J. Rossmeisl, and C. H. Christensen, "Towards the computational design of solid catalysts," *Nat. Chem.*, vol. 1, no. 1, pp. 37–46, Apr. 2009, doi: 10.1038/nchem.121.
[51] C. Kim *et al.*, "Blue TiO_2 Nanotube Array as an Oxidant Generating Novel Anode Material Fabricated by Simple Cathodic Polarization," *Electrochimica Acta*, vol. 141, pp. 113–119, Sep. 2014, doi: 10.1016/j.electacta.2014.07.062.

[52] S. Kim and C. Kim, “Phenol degradation on electrochemically self-doped TiO_2 nanotubes via indirect oxidation,” *Environ. Eng. Res.*, vol. 29, no. 2, pp. 230243–0, Jun. 2023, doi: 10.4491/eer.2023.243.
[53] J. Iniesta, “Electrochemical oxidation of phenol at boron-doped diamond electrode,” *Electrochimica Acta*, vol. 46, no. 23, pp. 3573–3578, Aug. 2001, doi: 10.1016/S0013-4686(01)00630-2.
[54] Y. Zhang *et al.*, “Optimized terbium doped Ti/PbO_2 dimensional stable anode as a strong tool for electrocatalytic degradation of imidacloprid waste water,” *Ecotoxicol. Environ. Saf.*, vol. 188, p. 109921, Jan. 2020, doi: 10.1016/j.ecoenv.2019.109921.
[55] C. Wang, L. Yin, Z. Xu, J. Niu, and L.-A. Hou, “Electrochemical degradation of enrofloxacin by lead dioxide anode: Kinetics, mechanism and toxicity evaluation,” *Chem. Eng. J.*, vol. 326, pp. 911–920, Oct. 2017, doi: 10.1016/j.cej.2017.06.038.
[56] A. Donaghue and B. P. Chaplin, “Effect of Select Organic Compounds on Perchlorate Formation at Boron-doped Diamond Film Anodes,” *Environ. Sci. Technol.*, vol. 47, no. 21, pp. 12391–12399, Nov. 2013, doi: 10.1021/es4031672.
[57] E. Borovinskaya, V. Khaydarov, N. Strehle, A. Musaev, and W. Reschetilowski, “Experimental Studies of Ethyl Acetate Saponification Using Different Reactor Systems: The Effect of Volume Flow Rate on Reactor Performance and Pressure Drop,” *Appl. Sci.*, vol. 9, no. 3, p. 532, Feb. 2019, doi: 10.3390/app9030532.
[58] W. Djoudi, F. Aissani-Benissad, and P. Ozil, “Flow modeling in electrochemical tubular reactor containing volumetric electrode: Application to copper cementation reaction,” *Chem. Eng. Res. Des.*, vol. 90, no. 10, pp. 1582–1589, Oct. 2012, doi: 10.1016/j.cherd.2012.02.003.
[59] Y. Pan *et al.*, “Preparation and characterization of Ti/SnO_2-Sb_2O_3/α-PbO_2/Ce-Nd-β-PbO_2 composite electrode for methyl orange degradation,” *J. Solid State Electrochem.*, vol. 24, no. 3, pp. 545–555, Mar. 2020, doi: 10.1007/s10008-019-04468-2.
[60] Q. Zhao, F. Wei, L. Zhang, Y. Yang, S. Lv, and Y. Yao, “Electrochemical oxidation treatment of coal tar wastewater with lead dioxide anodes,” *Water Sci. Technol.*, vol. 80, no. 5, pp. 836–845, Sep. 2019, doi: 10.2166/wst.2019.323.
[61] G. Arslan, B. Yazici, and M. Erbil, “The effect of pH, temperature and concentration on electrooxidation of phenol,” *J. Hazard. Mater.*, vol. 124, no. 1, pp. 37–43, Sep. 2005, doi: 10.1016/j.jhazmat.2003.09.015.
[62] Y. Wang, B. Gu, and W. Xu, “Electro-catalytic degradation of phenol on several metal-oxide anodes,” *J. Hazard. Mater.*, vol. 162, no. 2–3, pp. 1159–1164, Mar. 2009, doi: 10.1016/j.jhazmat.2008.05.164.
[63] F. Hu, X. Cui, and W. Chen, “Pulse Electro-codeposition of Ti/SnO_2–Sb_2O_4–CNT Electrode for Phenol Oxidation”.
[64] Y. Zheng, W. Su, S. Chen, X. Wu, and X. Chen, “Ti/SnO_2–Sb_2O_5–RuO_2/α-PbO_2/β-PbO_2 electrodes for pollutants degradation,” *Chem. Eng. J.*, vol. 174, no. 1, pp. 304–309, Oct. 2011, doi: 10.1016/j.cej.2011.09.035.
[65] P. Geng, J. Su, C. Miles, C. Comninellis, and G. Chen, “Highly-Ordered Magnéli Ti_4O_7 Nanotube Arrays as Effective Anodic Material for Electro-oxidation,” *Electrochimica Acta*, vol. 153, pp. 316–324, Jan. 2015, doi: 10.1016/j.electacta.2014.11.178.

[66] T. Wilke, M. Schneider, and K. Kleinermanns, "1,4-Hydroquinone is a Hydrogen Reservoir for Fuel Cells and Recyclable via Photocatalytic Water Splitting," *Open J. Phys. Chem.*, vol. 03, no. 02, pp. 97–102, 2013, doi: 10.4236/ojpc.2013.32012.
[67] J. Makuraza, "Vibrational and Electronic Spectra of Natural Dyes Constituents for Solar Cell Application: DFT and TDDFT Study," *Int. J. Mater. Sci. Appl.*, vol. 4, no. 5, p. 314, 2015, doi: 10.11648/j.ijmsa.20150405.16.
[68] P. Ravichandiran and S. Vasanthkumar, "Synthesis of heterocyclic naphthoquinone derivatives as potent organic fluorescent switching molecules," *J. Taibah Univ. Sci.*, vol. 9, no. 4, pp. 538–547, Oct. 2015, doi: 10.1016/j.jtusci.2014.12.003.
[69] L. Gui *et al.*, "Preparation and characterization of ZnO/PEG-Co(II)-PbO_2 nanocomposite electrode and an investigation of the electrocatalytic degradation of phenol," *J. Hazard. Mater.*, vol. 399, p. 123018, Nov. 2020, doi: 10.1016/j.jhazmat.2020.123018.
[70] L. Yu, J. Xue, L. Zhang, C. Tang, and Y. Guo, "Fabrication of a stable Ti/Pb-TiO_xNWs/PbO_2 anode and its application in benzoquinone degradation," *Electrochimica Acta*, vol. 368, p. 137532, Feb. 2021, doi: 10.1016/j.electacta.2020.137532.